



HAL
open science

Conditional Wavelet Technique Applied to Aircraft Data Measured in the Thermal Internal Boundary Layer During Sea-Breeze Events

Jean-Luc Attié, Pierre Durand

► **To cite this version:**

Jean-Luc Attié, Pierre Durand. Conditional Wavelet Technique Applied to Aircraft Data Measured in the Thermal Internal Boundary Layer During Sea-Breeze Events. *Boundary-Layer Meteorology*, 2003, 106 (3), pp.359-382. 10.1023/A:1021262406408 . hal-00137512

HAL Id: hal-00137512

<https://hal.science/hal-00137512>

Submitted on 11 Aug 2021

HAL is a multi-disciplinary open access archive for the deposit and dissemination of scientific research documents, whether they are published or not. The documents may come from teaching and research institutions in France or abroad, or from public or private research centers.

L'archive ouverte pluridisciplinaire **HAL**, est destinée au dépôt et à la diffusion de documents scientifiques de niveau recherche, publiés ou non, émanant des établissements d'enseignement et de recherche français ou étrangers, des laboratoires publics ou privés.



Distributed under a Creative Commons Attribution 4.0 International License

CONDITIONAL WAVELET TECHNIQUE APPLIED TO AIRCRAFT DATA MEASURED IN THE THERMAL INTERNAL BOUNDARY LAYER DURING SEA-BREEZE EVENTS

JEAN-LUC ATTIE¹ and PIERRE DURAND²

¹ *Laboratoire d'Aérodynamique, UMR CNRS-UPS 5560, Toulouse, France;* ² *Météo France, CNRM, URA-CNRS 1357, 42 Av. Coriolis, Toulouse, France*

Abstract. We describe a wavelet-based technique to determine the spectral turbulent contribution to the vertical flux of sensible heat in a position-wavelength representation. This technique combines a wavelet transform (Morlet wavelet) with conditional sampling. We apply this method to aircraft data collected during a sea-breeze circulation (BEMA97 experiment) with heterogeneous turbulence conditions horizontally and vertically as well. The turbulent fluxes are analysed with the conditional wavelet technique as a function of the wavelength and the horizontal distance. The turbulent processes within the thermal internal boundary layer associated with the sea breeze are clearly identified. The results exhibit the wavelength bands through which the upward flux (originating from the surface) and the downward flux (originating from the top of the boundary layer) are important.

Keywords: Conditional sampling, Sea breeze, Thermal internal boundary layer, Turbulent flux, Wavelet analysis.

1. Introduction

The analysis of turbulent signals in the atmospheric boundary layer requires various mathematical tools in order to translate the erratic behaviour of the time-series into statistical parameters. Among these tools, the statistical moments of various orders are the most widely used, because they relate a unique value (the moment) to a physical characteristic of the signals: the variance represents the turbulent energy, the skewness the asymmetry, whereas higher-order moments express the relative importance of extreme events with respect to the 'background' of the signal. In the same way, for coupled signals, correlation and covariance express their common behaviour, and if one signal is a velocity, the covariance is proportional to the turbulent flux along the direction of this velocity.

However, this analysis does not describe the 'nature' of the signals (a complete description would require an infinite number of moments). In particular, the characteristic scales of two signals could be very different even if the low-order moments are identical. To address this, auto covariance, cross-covariance and energy spectra analyses have been widely used, mainly since the rapid improvement of computer performance.

This scale analysis obtains characteristics valid only for the whole sample. It is not possible to deduce how the local characteristic scales vary along the sample either in amplitude, or in phase. As most atmospheric signals are inhomogeneous, studying the local characteristics of samples is crucial for many problems. Recent tools such as a wavelet transform are now applied to turbulence signals allowing a local spectral analysis. A wavelet transform is more applicable than a Fourier transform for analyzing inhomogeneous samples, such as time-varying signals recorded at ground-based platforms, or horizontally-varying signals recorded on-board instrumented aircraft. Over the last ten years, a lot of work has emphasized the power of this technique for surface- and boundary-layer turbulence analyses (see for instance, Mahrt, 1991; Collineau and Brunet, 1993; Hudgins et al., 1993; Druilhet et al., 1994).

Because turbulence is a powerful mechanism for momentum, mass and energy transfer (mainly along the vertical coordinate), turbulent fluxes are an integral feature of the surface energy budget, entrainment at the top of the boundary layer, and also the turbulent kinetic energy budget, which involves the momentum and buoyancy fluxes through the mechanical and buoyancy source terms, respectively. Improvement in the analysis of these turbulent transfers, from turbulent time (or space) series recorded in stationary (or horizontally homogeneous) conditions to more complex and realistic situations, requires tools able to provide a time-scale (or position-wavelength) representation. On the other hand, it is now well known that atmospheric turbulence is far from being a pure random uncorrelated process, and that coherent motions are present in turbulent signals to varying degrees, mainly when turbulent fluxes are important. Numerous studies based on conditional sampling techniques have demonstrated this fact.

We describe, in this paper, a new technique capable of giving information of both efficient wavelength and contribution to the flux. This method, termed conditional wavelet technique (CWT), combines wavelet analysis and conditional sampling. We focus on the vertical flux of sensible heat, which is critical to the distinction of the thermal internal boundary layer (TIBL), the entrainment zone (EZ) and the atmosphere above (Galmarini and Attié, 2000; hereafter GA2000). We use data collected in inhomogeneous turbulent conditions during a sea-breeze circulation that classically develops a TIBL. The data were obtained from an instrumented aircraft at different levels during the BEMA97 (Biogenic Emissions over the Mediterranean Area, June 1997) campaign over the coast of Spain, within and at the top of a TIBL.

The second section briefly describes the aircraft used to collect the data, its measurements system and data processing. The third section describes the CWT. Following this, the method is applied to data samples from June 9, 1997 (Section 4). At last, Section 5 describes the TIBL structure via the CWT applied to the whole data samples available from the BEMA97 experiment.

2. The Measurements

Several experiments were conducted in the Mediterranean area in the framework of the BEMA project (Seufert, 1997), whose main objective was to identify the role of biogenic emissions on tropospheric ozone production. Among these experiments, the last one was conducted in 1997 on the eastern Spanish coast, to the north of the city of Valencia (see Figure 1). From 9th to 13th of June, several flights were performed within sea-breeze circulations. However, we do not deal in this paper with the reactive chemical side of the experiment, and focus only on thermodynamics, dynamics, and ozone (used as an unreactive tracer) measurements.

The French research aircraft used was a twin-propeller Fokker 27, flying at about 90 m s^{-1} in the boundary layer. It is equipped with a radome, i.e., the nose of the aircraft has pressure ports measuring total pressure, attack and sideslip angles. Static pressure, as well as fast temperature and moisture, are measured on the fuselage, and fast and reference ozone sensors are installed inside the airplane. More details on the instrumentation, acquisition and data processing can be found in Lambert and Durand (1999), and in GA2000. After anti-aliasing filtering, the fast-response sensors are recorded at a rate of 64 s^{-1} , but the time-series are reduced to 16 s^{-1} for turbulence calculations. Given the airspeed of the airplane, wavelengths greater than 5 m can thus be captured, which is sufficient to resolve most of the turbulence energy in the boundary layer. The variables used hereafter, such as the three wind components, temperature, absolute humidity and ozone, were obtained in that way.

The continental part of the flight plan consisted of two perpendicular tracks of about 30 km length with one track parallel to the shoreline. The terrain elevation was slowly increasing from the shore inland, up to about 150 m at the inland innermost point. At this point, the surface was more complex, with alternating valleys and hills (Figure 1). Moreover, the flight plans consisted of vertically stacked straight and level runs, on the one hand perpendicular to the shore (DC in Figure 1), with an extension of the lowest flight leg 30 km over the sea (CS), and on the other hand parallel to the shore, over the track AA' located about 5 km inland. The flight altitudes of these legs ranged between 150 and about 1000 m a.s.l., the upper level depending on the thickness of the TIBL. Moreover, spiral profiles were flown at D, C, and S up to about 2000 m a.s.l.

3. Conditional Wavelet Technique

The CWT is based on wavelet transform combined with conditional sampling. The goal is to exhibit the sign of the contribution to the flux in a position-wavelength representation. For this, we used the Morlet wavelet (Grossman and Morlet, 1984) defined as:

$$\Psi(\eta) = \pi^{-1/4} e^{i\omega_0\eta} e^{-\eta^2/2}, \quad (1)$$

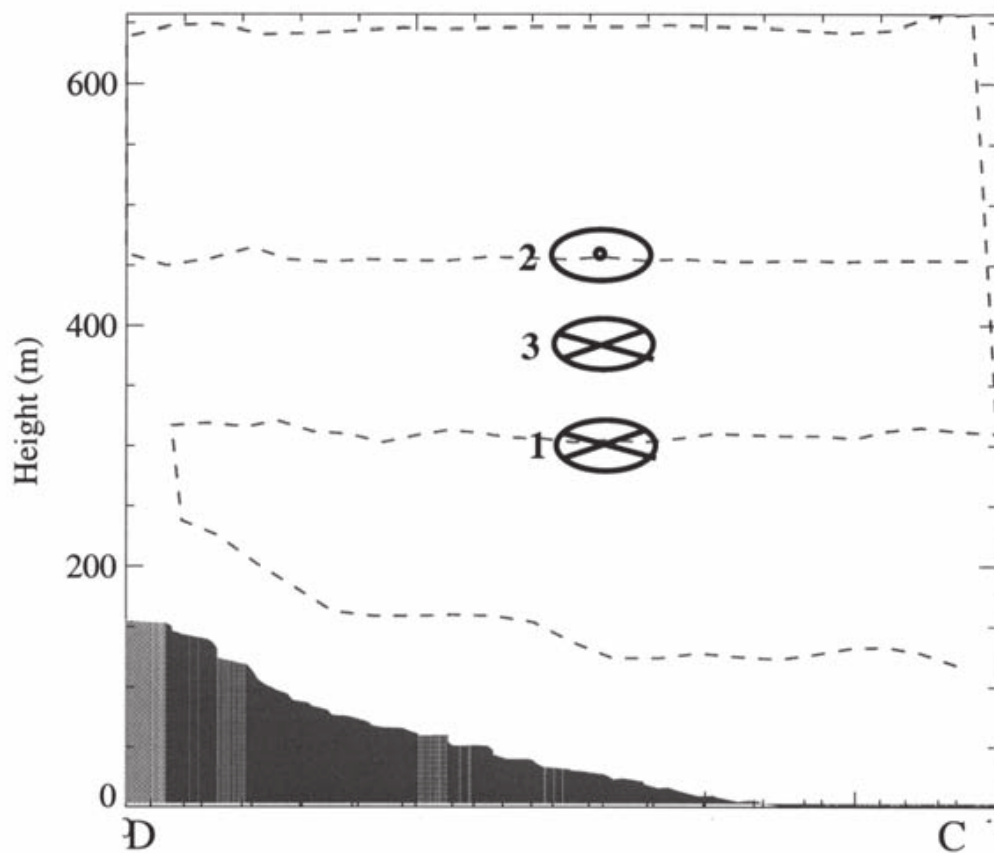
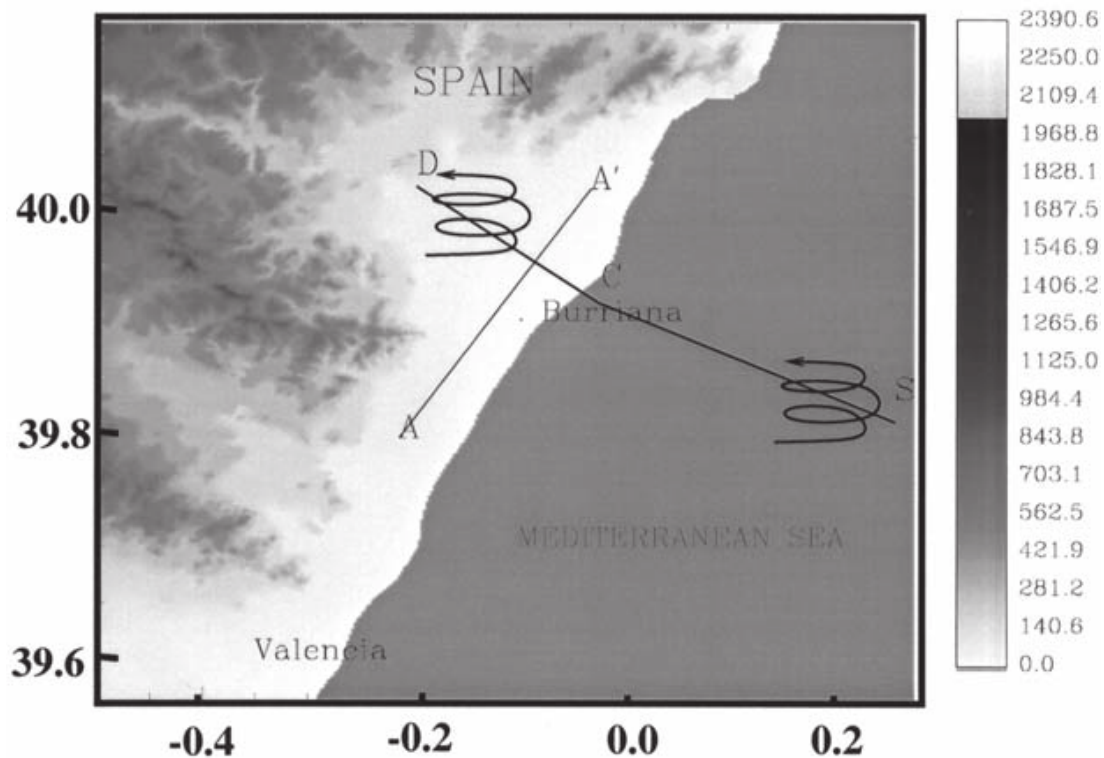


Figure 1. (Top) Map of the topography of the eastern coast of Spain where the BEMA97 campaign took place. The two lines indicate the transects of the aircraft perpendicular and parallel to the coast. The colour bar gives the height of topography (in m) and the spirals indicate the location of aircraft profiles. (Bottom) Flight pattern performed by the aircraft. Numbered ellipses represent runs parallel to the shoreline (1 and 3 are from A to A' and 2 is from A' to A).

where ω_0 is the non-dimensional frequency with $\omega_0 = 6$ satisfying the admissibility condition (Farge, 1992), η is a non-dimensional time parameter and $\Psi(\eta)$ is the wavelet function. The continuous wavelet transform of a discrete series x_n is defined as:

$$W_n^x(s) = \sum_{n'=0}^{N-1} x_{n'} \Psi^* \left(\frac{(n' - n)\delta t}{s} \right), \quad (2)$$

where s is the wavelet scale, n the localized time index, “*” indicates the complex conjugate, N is the number of elements of the discrete series and δt the time between two consecutive elements. Therefore, we can construct an image displaying the amplitude of the series in a time-scale or in a position-wavelength representation (assuming Taylor’s hypothesis, since each time step and scale corresponds to a position and a wavelength, respectively).

In the same way, we calculate the spectral energy in a position-wavelength representation defined as:

$$E_n^x(s) = W_n^x(s) W_n^{x*}(s). \quad (3)$$

In addition, a statistical significance test (based on the χ^2 test) defines the areas in the position-wavelength representation with a 95% statistical confidence, i.e., the probability for wavelet energy falling in a specific position-wavelength interval. The test assumes a χ^2 distribution of E_n , and although it is derived for homogeneous signals (Torrence and Compo, 1998), it allows the selection of wavelet scalogram portions that are statistically significant.

We also calculate the covariance (which expresses the vertical turbulent flux, for example, if one of the two signals is the vertical velocity) as the multiplication of the wavelet real parts of two variables. For instance, for potential temperature $W_n^\theta(s)$ and vertical velocity $W_n^w(s)$, it is calculated as:

$$C W_n^{w,\theta}(s) = W_n^w(s) W_n^\theta(s). \quad (4)$$

The image obtained is called a wavelet cross-spectrum and shows the flux in the position-wavelength representation. Using different colours for different signs of the variable contribution, we obtain a representation of both the flux intensity and variable sign in a position-wavelength frame. Such a representation combines conditional sampling and the wavelet analysis (Attié et al., 1995; Druilhet and Durand, 1997). For example, Figure 2 shows the sensible heat flux measured at about 100 m a.s.l.. The upper diagram presents the time-series of the instantaneous flux and its time integral (eddy-correlation method). The integral of the flux continuously increases following a fairly straight line, indicating a homogeneous flux (Durand et al., 1988). The intermediate diagram shows the standard cross-scalogram of the vertical velocity and the potential temperature while the bottom

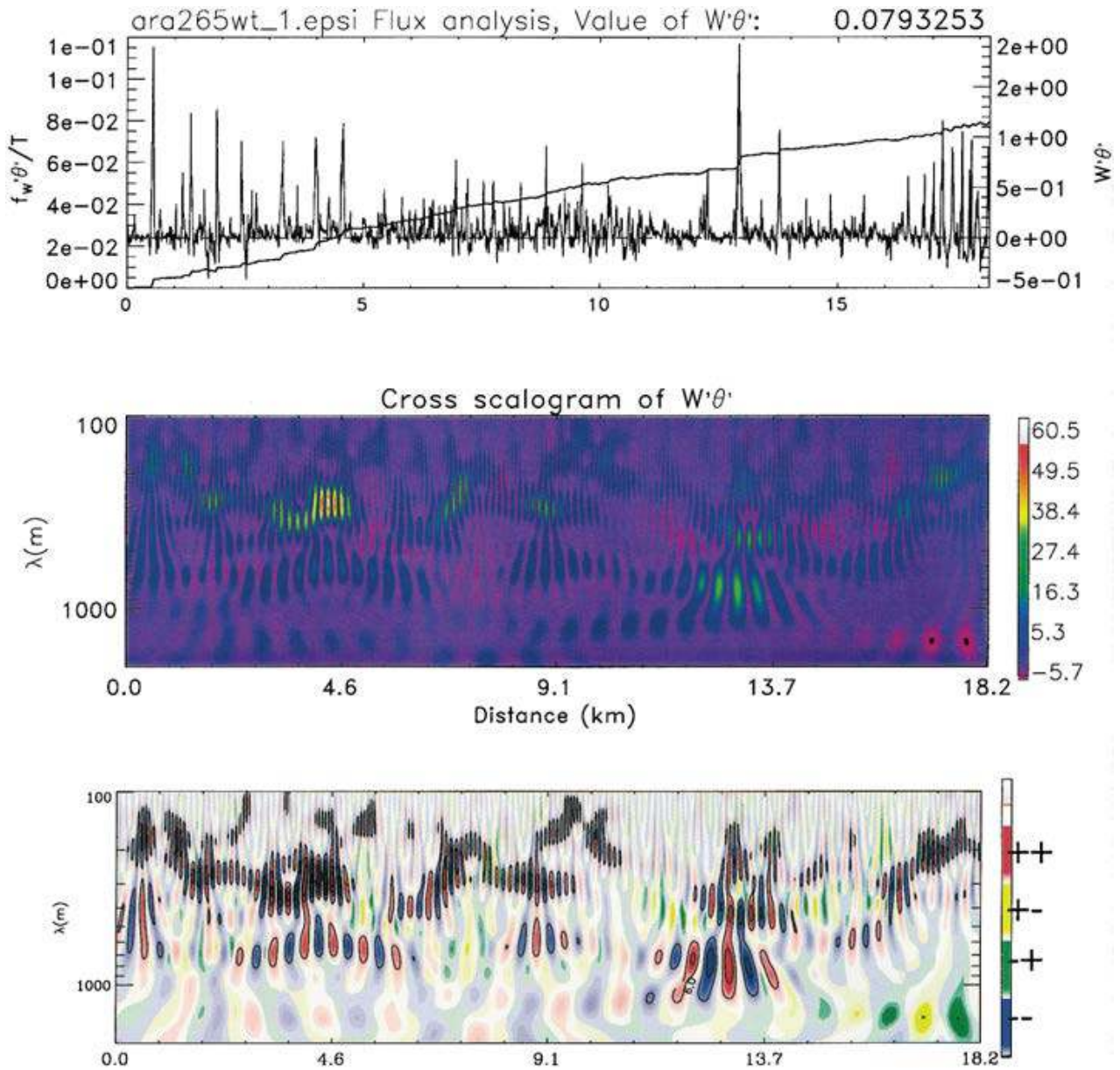


Figure 2. Aircraft measurements along a constant level flight parallel to the shoreline (between A and A'). This flight has been performed on June 12, 1997 at 1330 UT at 100 m a.s.l over orange-tree groves. Product of w' and θ' and corresponding integral of $w'\theta'$ (top). Standard cross-scalogram corresponding to $w'\theta'$ (middle); The colourbar indicates the intensity of $w'\theta'$. Conditional wavelet cross-scalogram contoured by values from the standard cross-scalogram (bottom); the colourbar indicates the sign of the fluctuations (++ for $w' > 0$ and $\theta' > 0$; +- for $w' > 0$ and $\theta' < 0$; -+ for $w' < 0$ and $\theta' > 0$; -- for $w' < 0$ and $\theta' < 0$).

diagram displays the associated conditional wavelet cross-scalogram. The standard cross-scalogram shows high amplitude areas corresponding to positive transfer, and homogeneously distributed in the wavelength range of 100 m to 800 m. Similarly, the cross-scalogram also shows the sign of each variable contribution. A majority of both red (positive contribution of w' and θ') and blue (negative contribution of w' and θ') areas indicates an upward sensible heat flux. The contour lines delineate the observed intensity of flux at each position-wavelength location.

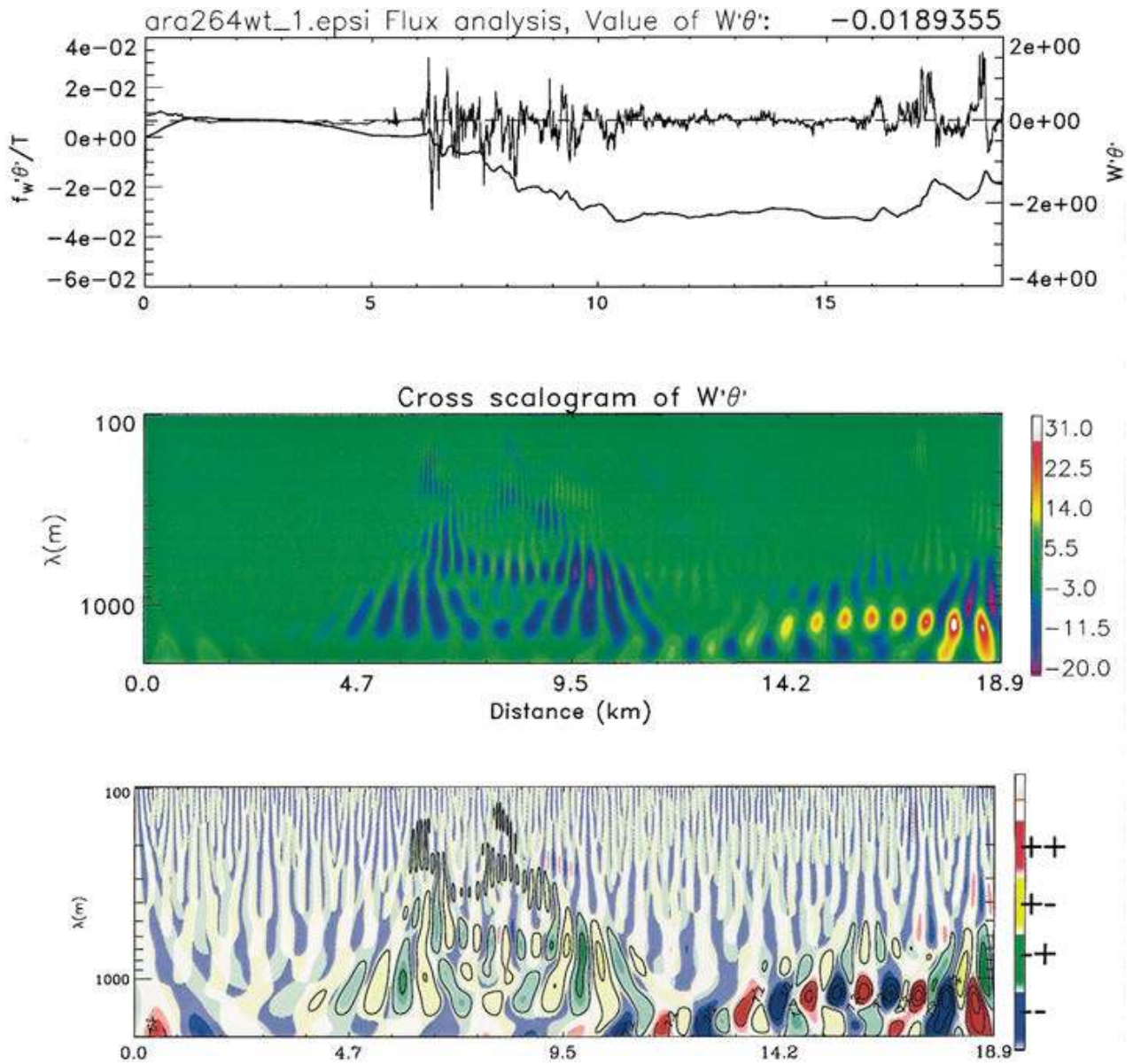


Figure 3. Same as Figure 2 but for a constant level flight performed at 1320 UT at 450 m a.s.l perpendicular to the shore.

Conversely, when the data are collected close to the EZ, and thus when the sensible heat flux is negative (Figure 3), a majority of yellow and green areas occur. Yellow colour areas correspond to positive and negative fluctuations of w' and θ' , respectively, whereas green colour areas correspond to negative and positive fluctuations of w' and θ' , respectively. One can notice that the time integral of the flux (upper diagram) is not a straight line, indicating an inhomogeneous time-series. The figure points out the location of the EZ crossed by the aircraft between 6 and 11 km on the x-axis.

Therefore, the CWT differentiates the contribution of turbulent variable (positive and negative) localized in a position-wavelength representation.

4. Mean Flow on June 9, 1997

Figure 4 shows the profiles of horizontal wind vector, potential temperature, moisture and ozone on June 9, 1997 (one between D and C over the land and one over the open sea named SEA). Each profile covers a cylinder of about 1 km diameter and is located on the line perpendicular to the shore. The profiles of horizontal wind vectors show a westerly wind flow in the lower layer up to 800 m a.s.l. with mean windspeed values of 10 m s^{-1} . Above this altitude, at about 1800 m a.s.l., the wind rotates northwards indicating the direction of the synoptic flow.

The profiles of potential temperature and moisture indicate a variation at about 400 m a.s.l. over the land and 200 m a.s.l. over the sea. This shows the internal structure of the breeze that marks the TIBL top over the land and the marine boundary-layer (MBL) top over the sea. In addition, the ozone variations are strongly correlated with those of moisture and temperature. The ozone profile also indicates another maximum between 1000 and 1200 m a.s.l., in the wind shear, probably related to a plume advected over the area.

A first remark based on these figures is that the flow direction is not exactly perpendicular to the shoreline, but the structure of a breeze is described. Then, we identify a standard sea-breeze circulation illustrated by flow from the open sea to the land with a depth of about 800 m, a shear flow layer of almost 900 m depth in which the flow rotates from west to north, and a return-flow layer where the direction is towards the sea (synoptic flow).

5. Thermal Internal Boundary-Layer Structure

In this section, we analyse the structure of the TIBL from the vertically stacked flight legs, performed normal and parallel to the shoreline on June 9, 1997.

5.1. PERPENDICULAR FLIGHT LEGS

Figures 5a,b and c show the fields of potential temperature, moisture and ozone over the land obtained from data collected during a shoreline-normal flight plan. The figures clearly depict a typical internal structure delineated by a maximum in the vertical temperature gradient, and by a larger vertical gradient of moisture and ozone, whereas within the bulk of the TIBL these quantities are vertically homogeneous.

Figure 6 presents the time-series of the vertical velocity measured on four normal flight legs performed at heights of 650, 450, 300 and 150 m a.s.l.. One can see the location from the shoreline at which the aircraft enters the TIBL, according to the altitude, by the sudden increase of the turbulence intensity: it is about 12 km at 650 m a.s.l., 7 km at 450 m a.s.l., 3 km at 300 m a.s.l., whereas the lowest flight leg passes from the marine to the continental boundary layer without a strong increase in turbulence level.

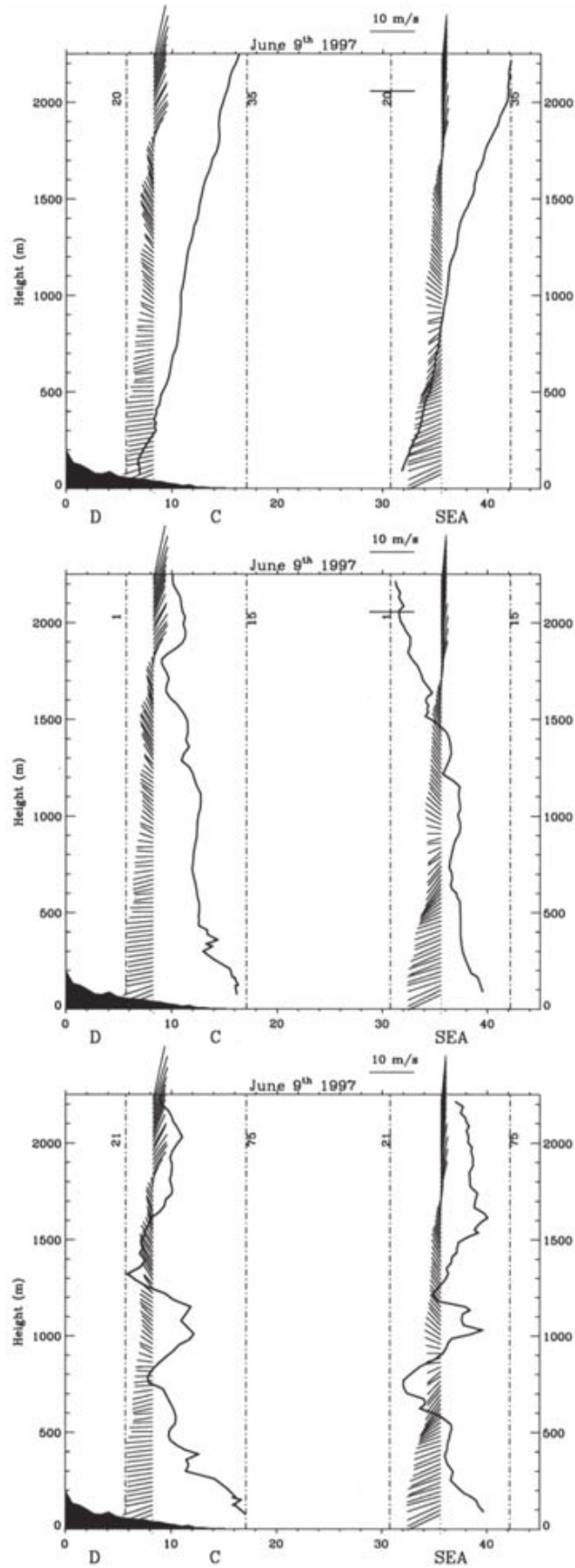


Figure 4. Profiles of wind, specific humidity, potential temperature and ozone on June 9, 1997 at noon. (Top) Potential temperature (range in $^{\circ}\text{C}$ along the vertical dashed line) and wind vectors; (middle) moisture (range in g kg^{-1} along the vertical dashed line) and wind vectors; (bottom) ozone concentration (indicated in ppbv along the vertical dashed lines) and wind vectors.

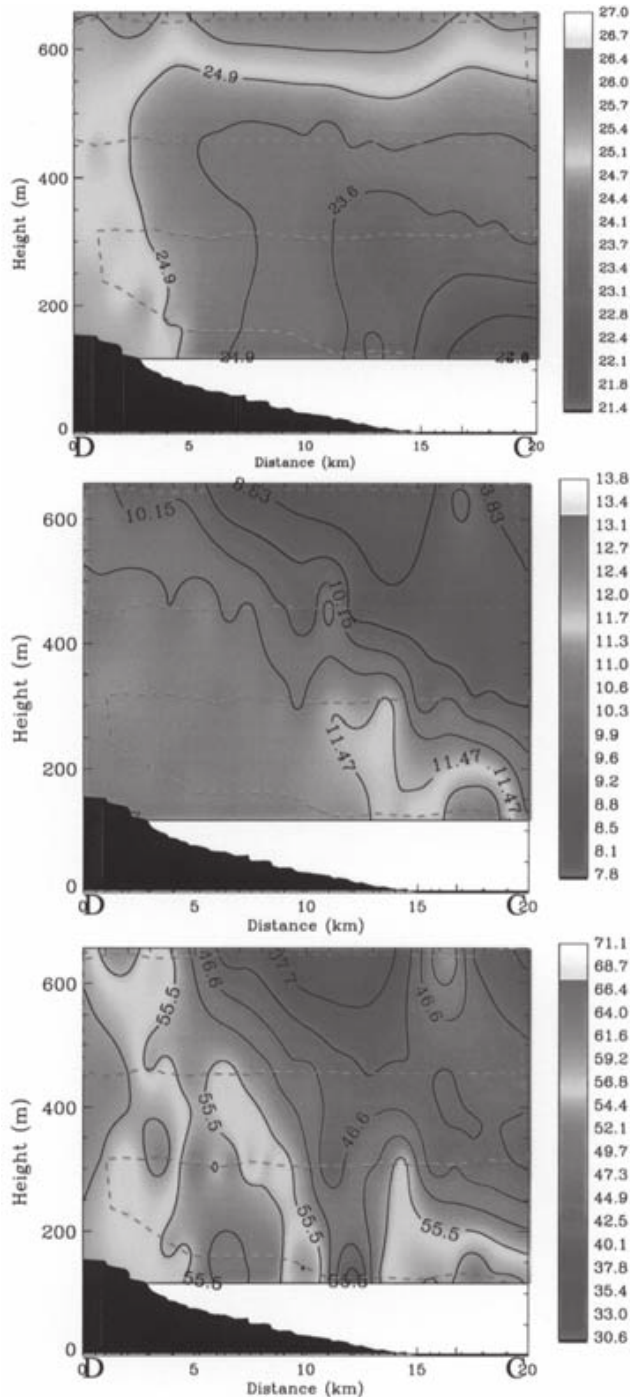


Figure 5. Potential temperature (in $^{\circ}\text{C}$) (top), moisture (in g kg^{-1}) (middle) and ozone (in ppbv) (bottom) fields over the land computed from data collected during the flight plan perpendicular to the shoreline on June 9. The dashed lines indicate the different vertically stacked flight legs performed by the aircraft. The bottom shaded area indicates the overflight topography.

Figure 7 shows the wavelet energy of the vertical velocity time-series presented in Figure 6. In a typical convective boundary layer (CBL), it is generally assumed that the wavelength of the energy-containing eddies increases with altitude in the lowest part of the CBL, then reaches an asymptotic value that is slightly greater than the CBL thickness (Kaimal and Finnigan, 1994). We would therefore expect this wavelength to increase with the distance from the shore in the bulk of the TIBL. This characteristic is evident only on the lowest flight leg, for which a

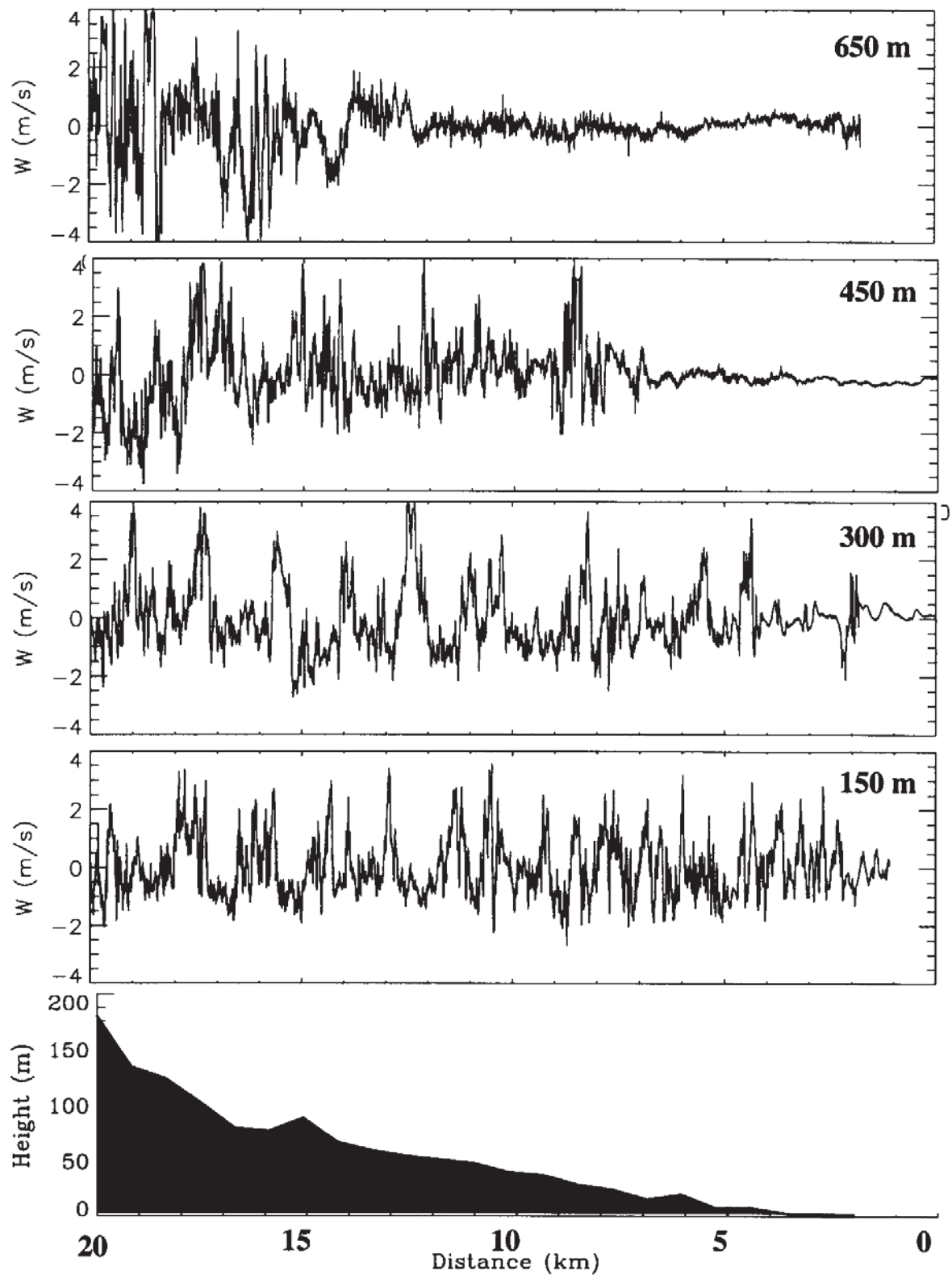


Figure 6. Vertical velocity in m s^{-1} measured by the aircraft at four levels (100, 300, 450 and 650 m a.s.l.) perpendicular to the shoreline. The bottom shaded area represents the overflown topography.

wavelength with high energy increases from 700 m at 8 km from the shore, to about 1500 m at 16 km. This behaviour is contoured by the 95% confidence interval and is therefore reliable. The three other diagrams do not reproduce the same behaviour, which can be interpreted as follows: in the lower layers above the surface layer, the boundary-layer structure is controlled by surface fluxes (mainly buoyancy flux), as in the homogeneous CBL. Above that, the structure is strongly influenced by the exchanges at the TIBL top, amongst which entrainment plays a dominant role (GA2000). These exchanges are stronger than in a homogeneous boundary layer, because vertical transfers are increased by the horizontal advection of MBL air into the TIBL.

Some insight into the turbulent transfer through the TIBL can be gained via the conditional cross-scalogram related to the sensible heat flux for June 9 (Figure 8). The vertical dashed lines on the diagrams indicate the region that delineates the EZ, where a majority of green and yellow areas are seen, corresponding to downward flux. The lowest flight leg was in the EZ (of the MBL or the TIBL) up to 5 km from the shore inland. On the other hand the highest flight leg is in the EZ between 10 and 16 km from the shoreline. On the two intermediate flight legs, the EZ is localized between 3 and 7 km from the shore at 300 m a.s.l., and between 7 and 10 km at 450 m a.s.l. Anywhere else, the upward flux (red and blue areas) predominates, as can be seen on the left part of the two lower flight legs. It can also be noticed that the most energetic scales of the vertical velocity, which were put into evidence on the energy wavelet spectra (Figure 7), correspond to the efficient scales for the heat transfer.

The main characteristics of the internal boundary layer, as inferred from the CWT, are summarized in the scheme of Figure 9. This technique allows the distinction between the eddies transporting heat upwards, and originating from surface heat flux, and those transporting heat downwards and originating from the EZ. The size of the upward flux eddies increases according to the distance from the shoreline, because they are related to the boundary-layer thickness, which increases with this distance (see, for instance, on the lowest altitude run). From the most inland part of the four runs, it can be seen that the size of upward flux eddies increases with altitude up to the half of the boundary layer and remain constant above. Concerning the downward flux eddies, they originate from the EZ, and thus their size increases with the horizontal thickness of this area, i.e., with the distance from the shoreline. As far as we go away from the EZ downwards, the downward flux eddies become more and more scarce, as well as their size decreasing, because they are stretched between the most energetic eddies (this well known behaviour explains the negative values of the moisture skewness in the bulk of the CBL, as stressed out by Deardorff, 1974).

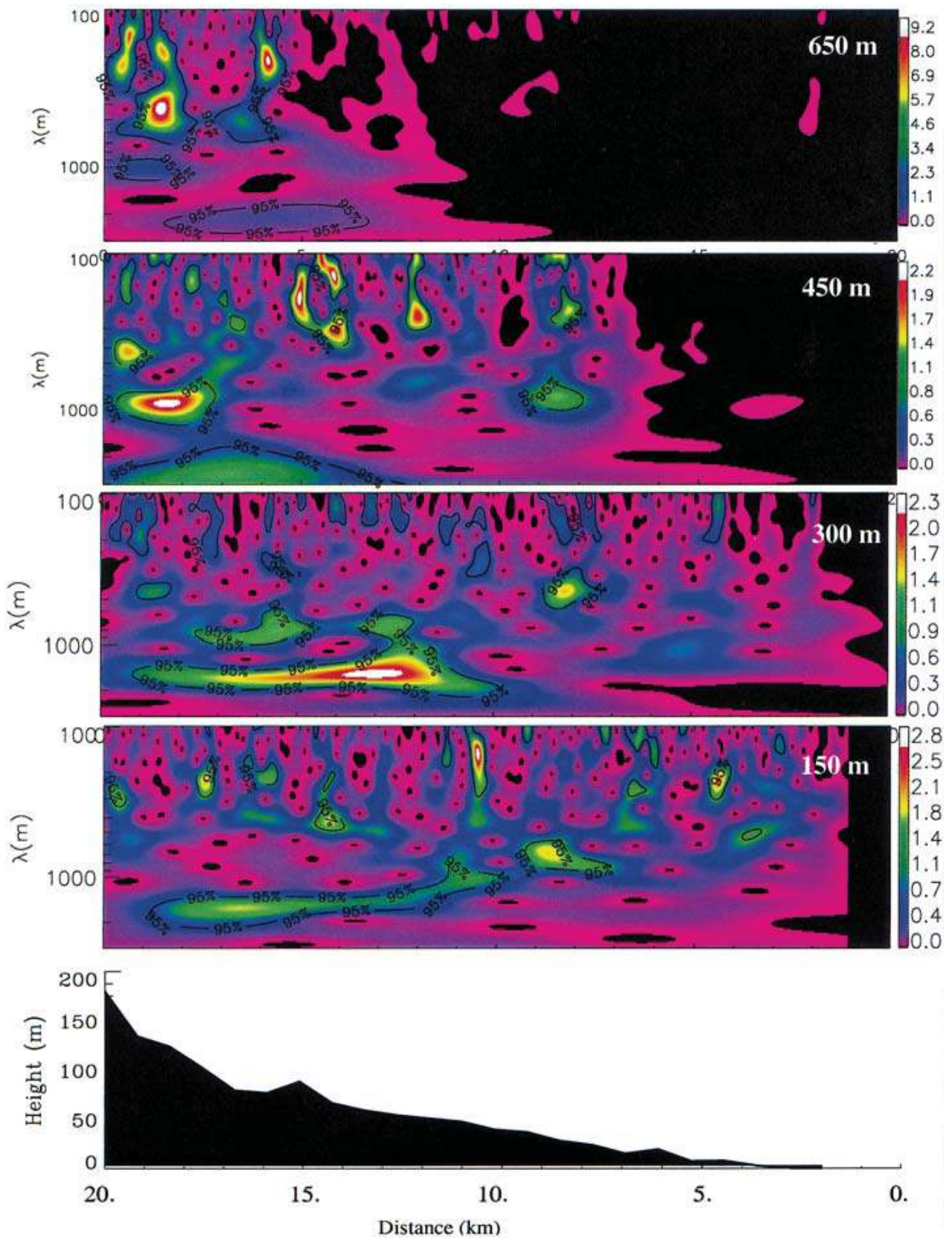


Figure 7. Wavelet transform of the vertical velocity shown in Figure 6. The scalograms show the energy times the frequency. The countourlines represent the 95% confidence interval. The bottom shaded area represents the overflow topography.

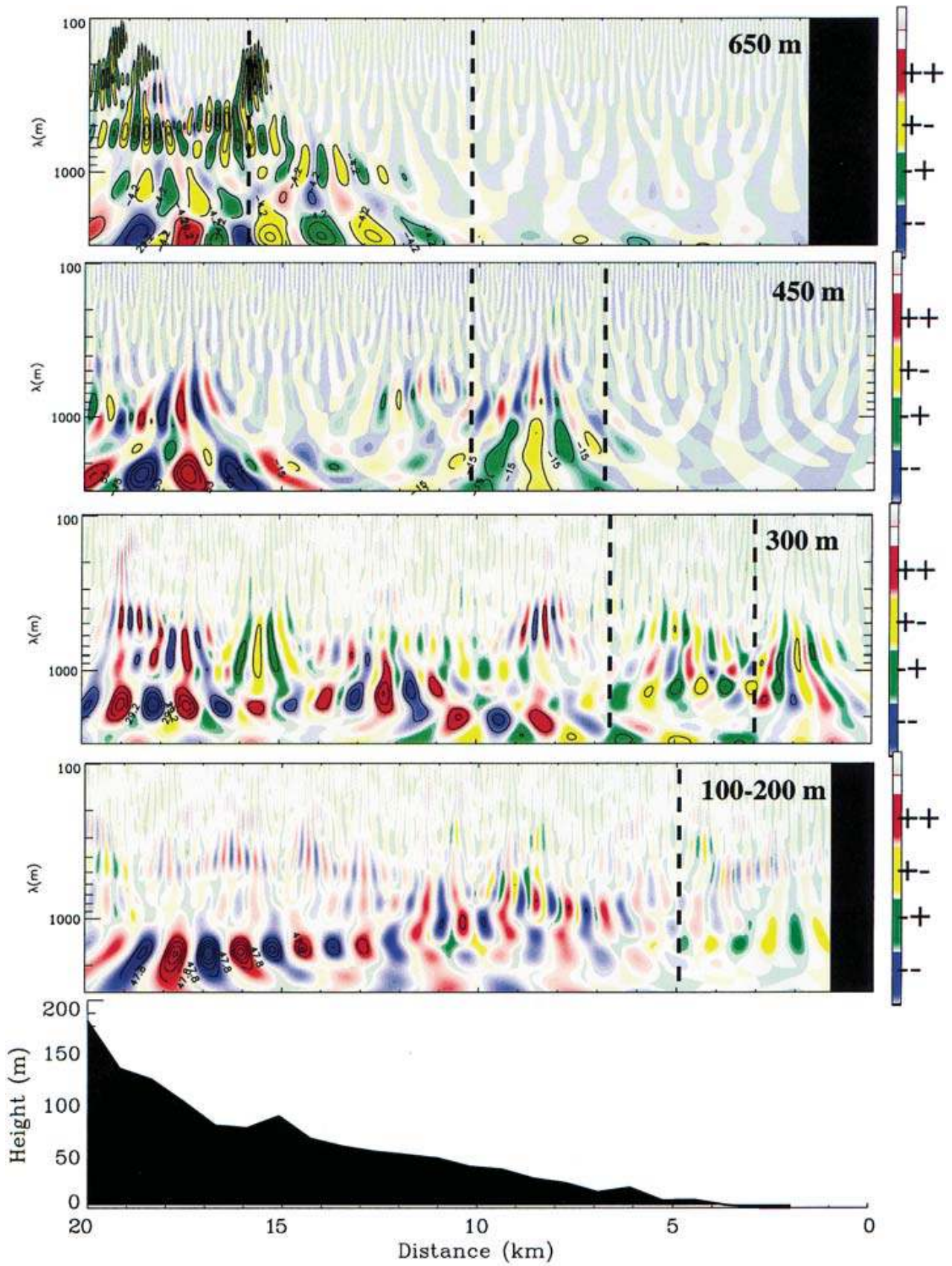


Figure 8. Conditional cross-scalogram of $w'\theta'$ at the same four levels normal to the shore. The isolines represent the value of the wavelet covariance. The bottom shaded area represents the overflown topography.

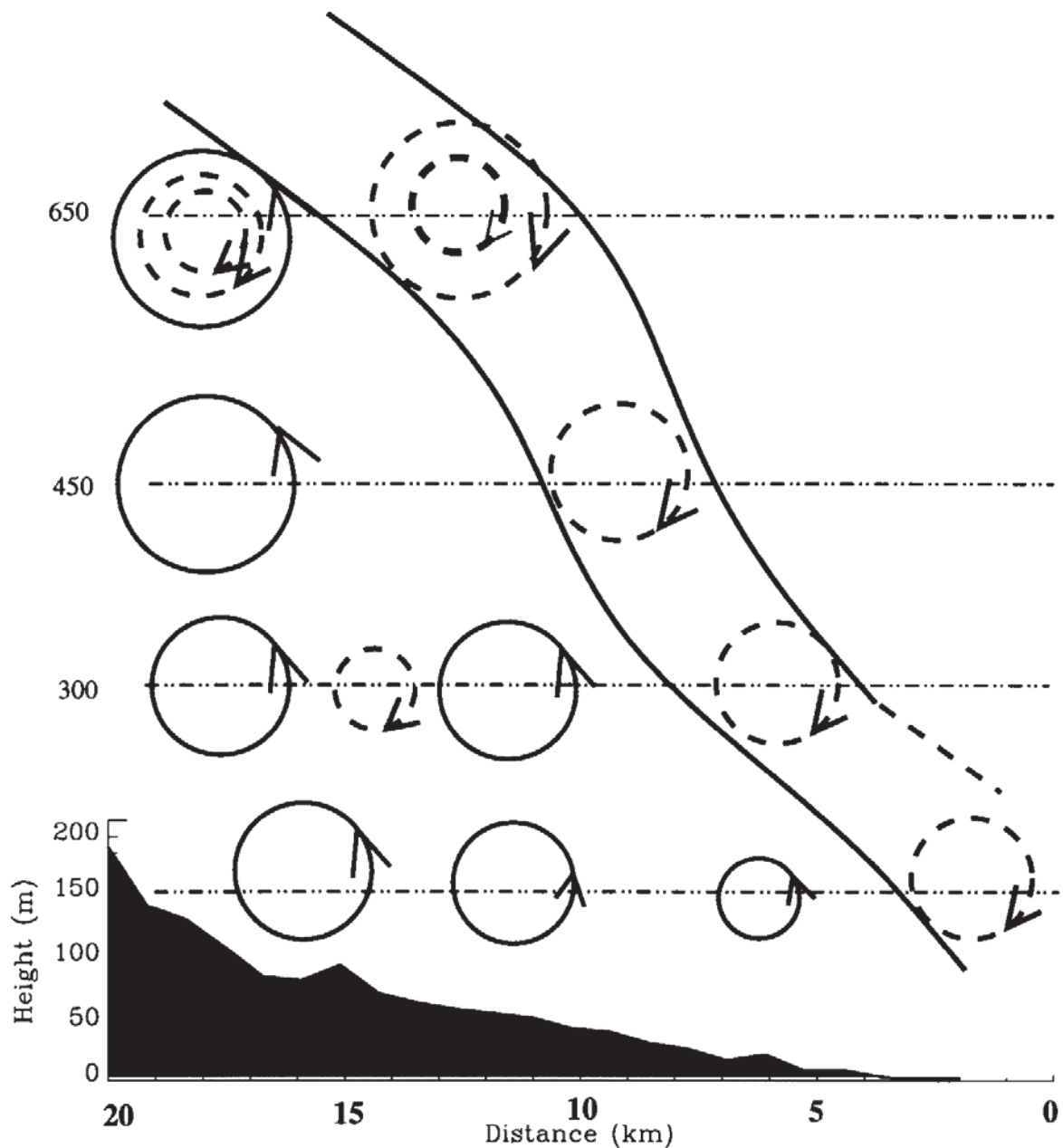


Figure 9. Scheme showing the location and size of downwards (dashed line circles) and upwards (full line circles) flux eddies as revealed by the CWT applied to aircraft data measured in the internal boundary layer. The full lines delineate the EZ.

5.2. PARALLEL FLIGHT LEGS

The same analysis was repeated for stacked flight legs performed parallel to the shore. Figure 10 presents the vertical velocities measured at heights of 300, 360 and 420 m a.s.l. However, the shoreline was not exactly a straight line, with the horizontal distance to the aircraft varying from 5.1 km to 3.2 km (at the end of the leg). The strongest vertical velocity fluctuations started at about 20 km on the x-axis corresponding to a minimum distance between the aircraft track and the shoreline. However, 75% of the sample run was between 3.5 and 4.5 km from the shore, with an average distance of about 4 km. Therefore, we assume that the effect of the shoreline shape is negligible. Moreover, Figure 11 does not exhibit sharp

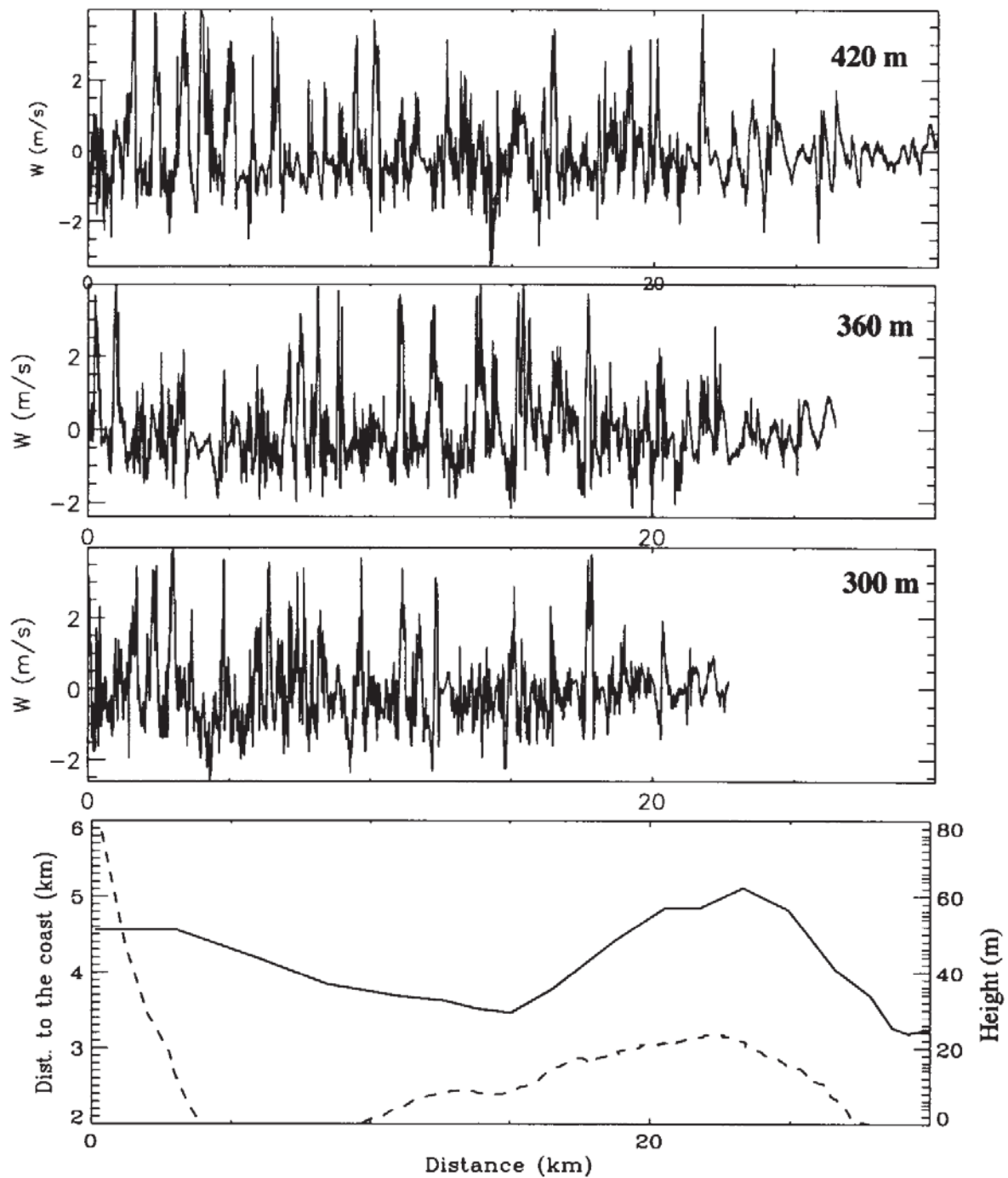


Figure 10. Vertical velocity (m s^{-1}) measured by the aircraft at three levels along runs parallel to the shoreline. The bottom diagram represents the topography height (dashed line) and the distance between the aircraft track and the shoreline (full line).

characteristics (compared to the features of the shoreline-normal plan). Between 2 and 6 km from the beginning of the legs, several coherent structures with a wavelength of about 800 to 900 m are probably responsible for the energy peak appearing on the scalograms of the upper and lower legs. These structures are visible on the corresponding time-series of the vertical velocity (see Figure 10). On the intermediate leg, the most energetic structures appear in the middle of the time-series, but with a greater wavelength (1000 to 2000 m).

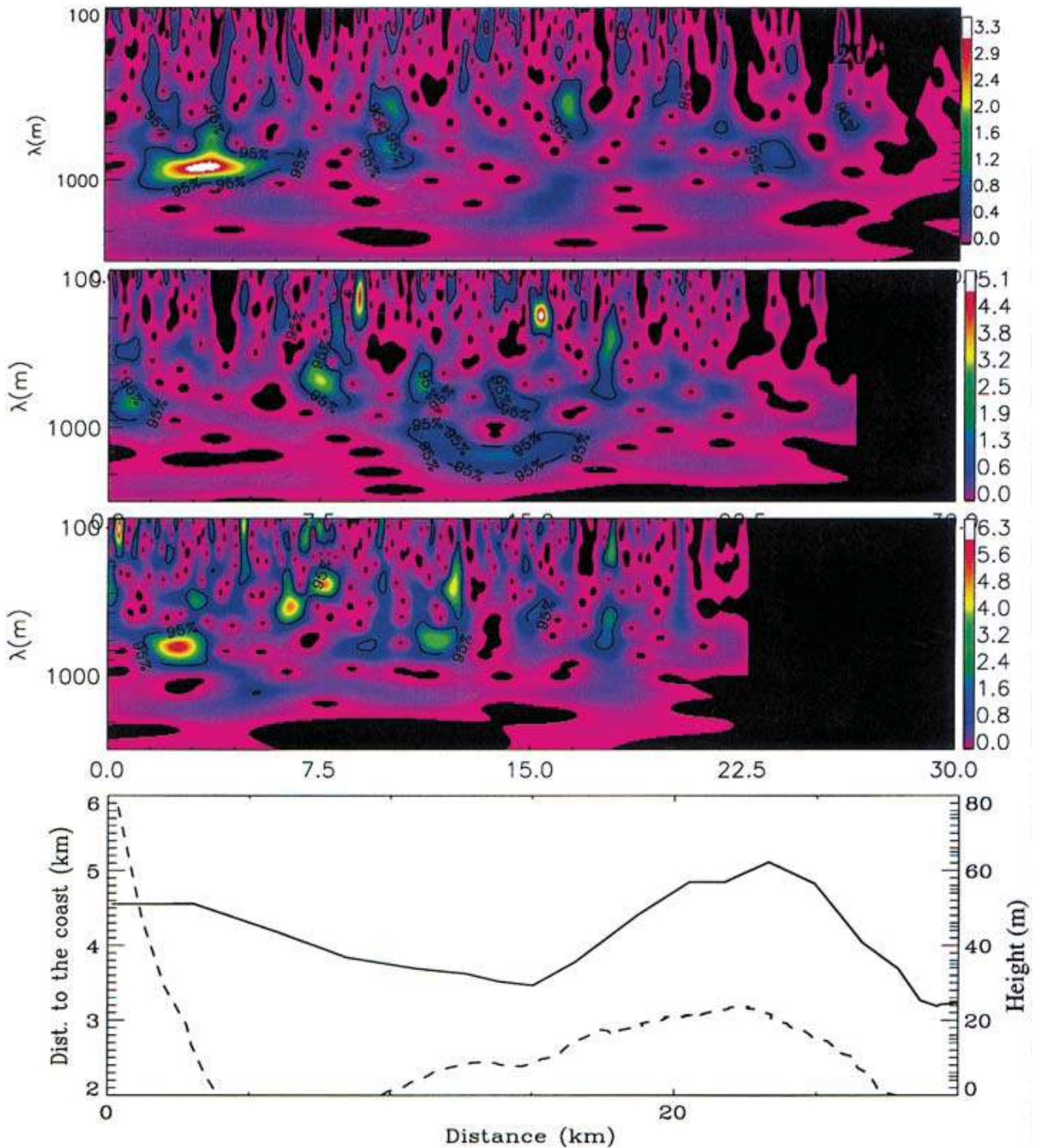


Figure 11. Wavelet transform (energy) times the frequency for the vertical velocity presented in Figure 10.

If we refer to Figure 12, the parallel-to-shore flight leg at 300 m a.s.l. should be in the EZ and the leg at 420 m a.s.l. should be above. In fact, Figure 12 shows that the 360 and 420 m a.s.l. parallel legs were within the EZ (a majority of green and yellow areas), whereas the 300 m a.s.l. leg was probably just below, as shown by alternating green-yellow ($w'\theta' < 0$) and red-blue ($w'\theta' > 0$) areas. The TIBL probably has slightly increased between measurements performed normal and parallel to the wind (later), coinciding with the reinforcement of the sea-breeze circulation at the beginning of the afternoon.

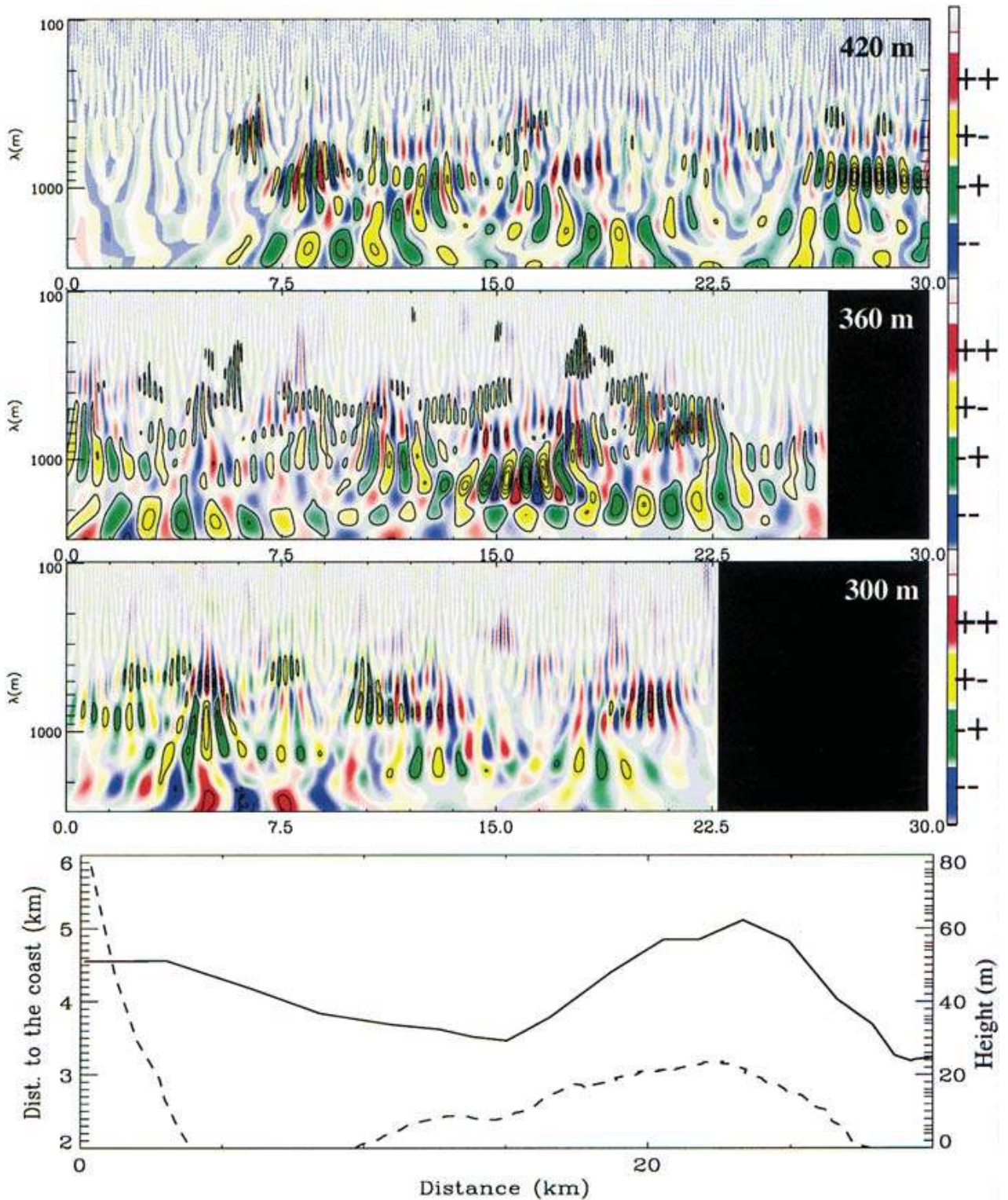


Figure 12. Conditional cross-scalogram of $w'\theta'$ computed from data measured in the plane parallel to the shore. The contour lines represent the value of the wavelet covariance.

The conditional cross-scalograms (Figure 12) present both a large band of scales and various contributions (positive and negative). The behaviour is significantly different from that observed on the normal legs in the areas right below the EZ (see Figure 8). However, on the normal legs, the EZ presents comparable features (large variety of scales and alternating of upward and downward flux). One can notice that the structures, evident at the beginning of the 420 m a.s.l. leg on the

vertical velocity, do not transfer sensible heat, and are probably related to gravity waves propagating in the upper stable layer.

5.3. CONDITIONAL WAVELET PROFILES

In order to quantify this behaviour between the bulk of the TIBL and the EZ, we calculated the quantity:

$$\overline{r_k} = \left(\frac{\sum_{i,j} w_i' \theta_j'}{\sum_{i,j} |w_i' \theta_j'|} \right)_{d,k}, \quad (5)$$

where i and j represent the sign of the fluctuation. The average is done over the flight track distance d for each wavelength k . This parameter shows the largest contribution to the sensible heat flux (upward or downward) according to the scale. A positive value means the upward flux is greater than the downward flux and vice versa. This shows the scale range and the proportion of upward or downward flux involved in the exchange. The aim is to identify the EZ in terms of wavelength and intensity. It could be interpreted as a normalized cospectrum (i.e., which does not depend on the flux value at any given wavelength), close to +1 (respectively -1) when the flux is upward (respectively downward) and well organized, and close to zero when the transfer vanishes. It resembles the cosine of the phase between the two signals in the Fourier transform.

Figures 13 and 14 show how this parameter behaves, at various altitudes, for normal and parallel flight legs, respectively. Three days are analyzed (June 9, 12 and 13), in order to demonstrate that some characteristic features are reproducible from one day to another. As for the June 9 case, the diagrams show a sea-breeze circulation, with a well developed TIBL. However, the altitudes of the stacked flight legs presented on these diagrams are not identical from one day to another. For example, on June 12, the upper cross-shore leg was flown at 450 m a.s.l., whereas it was at 600 m a.s.l. on the two other days. Also, on the parallel legs, the lowest leg was at 300 m a.s.l. on June 9, whereas this leg was at 100 m a.s.l. on the two other days. Tables I and II present the vertical velocity variance and the sensible heat flux values corresponding to the flight legs. It can be noticed that the upper leg generally has a weak downward heat flux, which confirms that this leg is in the EZ. However, the lowest flight legs (100 or 150 m a.s.l.) present a wide wavelength range of upward contribution to the flux. This appears on both the cross and parallel legs. This agrees with the classical picture of the surface-layer cospectrum, in which the surface fluxes (buoyancy) and the altitude are the relevant parameters for the organization of the transfer. These parameters do not vary significantly according to the distance to the shore, which explains similar behaviour of the heat transfer on normal and parallel flight legs.

The upper normal legs were flown in the EZ. The $\overline{r_k}$ parameter therefore is negative, but in a quite narrow wavelength band (compared to the lower flight legs).

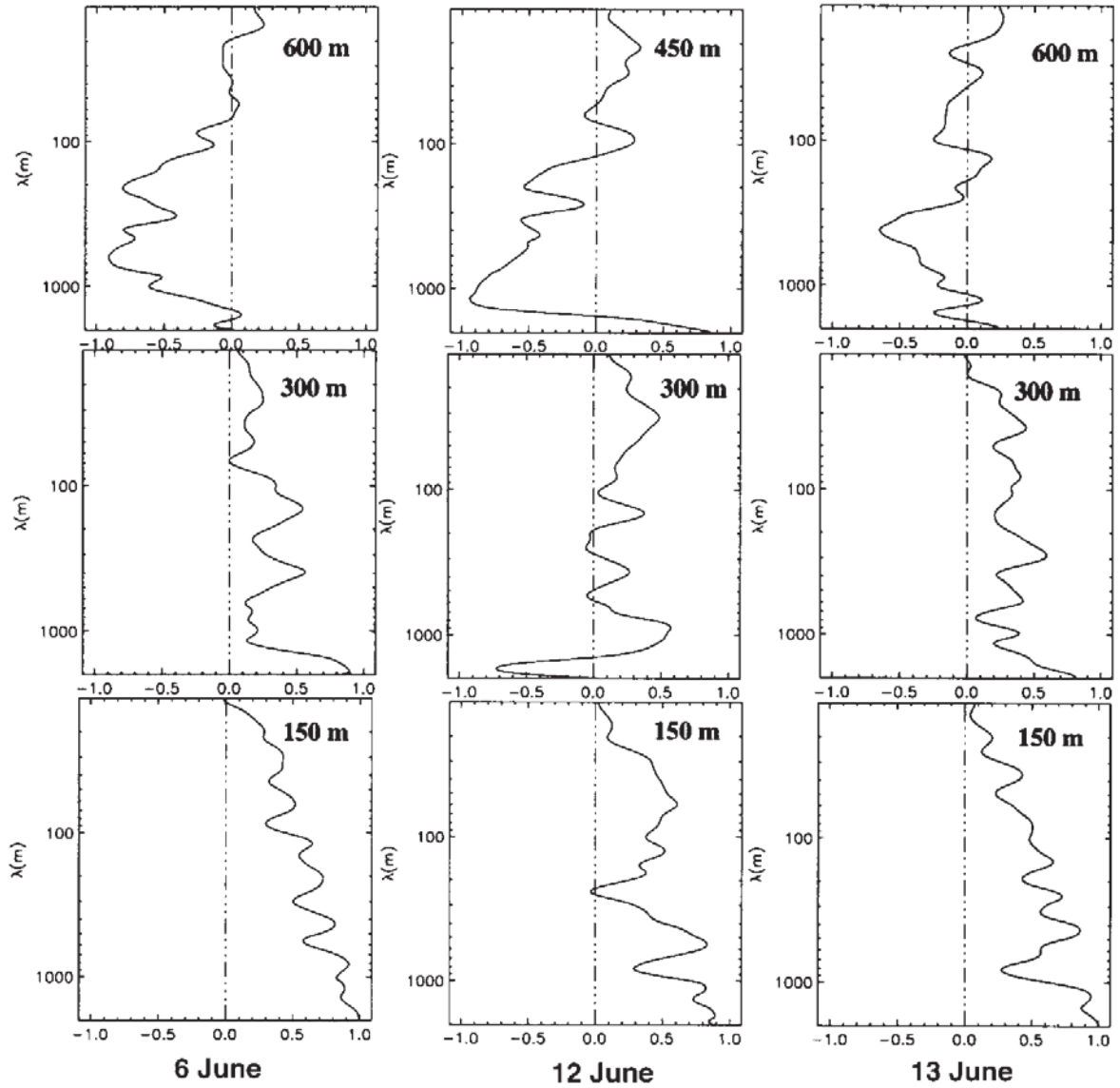


Figure 13. Average conditional wavelet profiles (parameter $\overline{r_k}$) for the normal flight legs on June 9, 12 and 13, 1997. These profiles are obtained from conditional cross scalograms.

The downward heat flux results from both the penetrative updrafts through the capping inversion, and the upper air parcels entrained into the CBL. These are coherent structures, rather than isotropic turbulence, which explains the narrowness of the wavelength band that contributes to the transfer. On the parallel flight legs, the same behaviour is observed, except for the June 12 case, where the upper leg lies below the EZ.

On the intermediate flight leg, both effects (upward flux from the surface, and downward flux from the CBL top) are competitive. The result is a mixed contribution, which could vary according to the situation and the altitude in the CBL. For example, on the parallel legs, the surface contribution is prominent at 180 m a.s.l. on June 12, whereas the contribution from the top appears on the 250 m a.s.l. leg for June 13. On June 9, at 300 and 360 m a.s.l., the upward contribution appears at shorter wavelengths, whereas the entrainment appears at wavelengths around 1000 m. Concerning the normal flight legs, the intermediate levels (300 m a.s.l.)

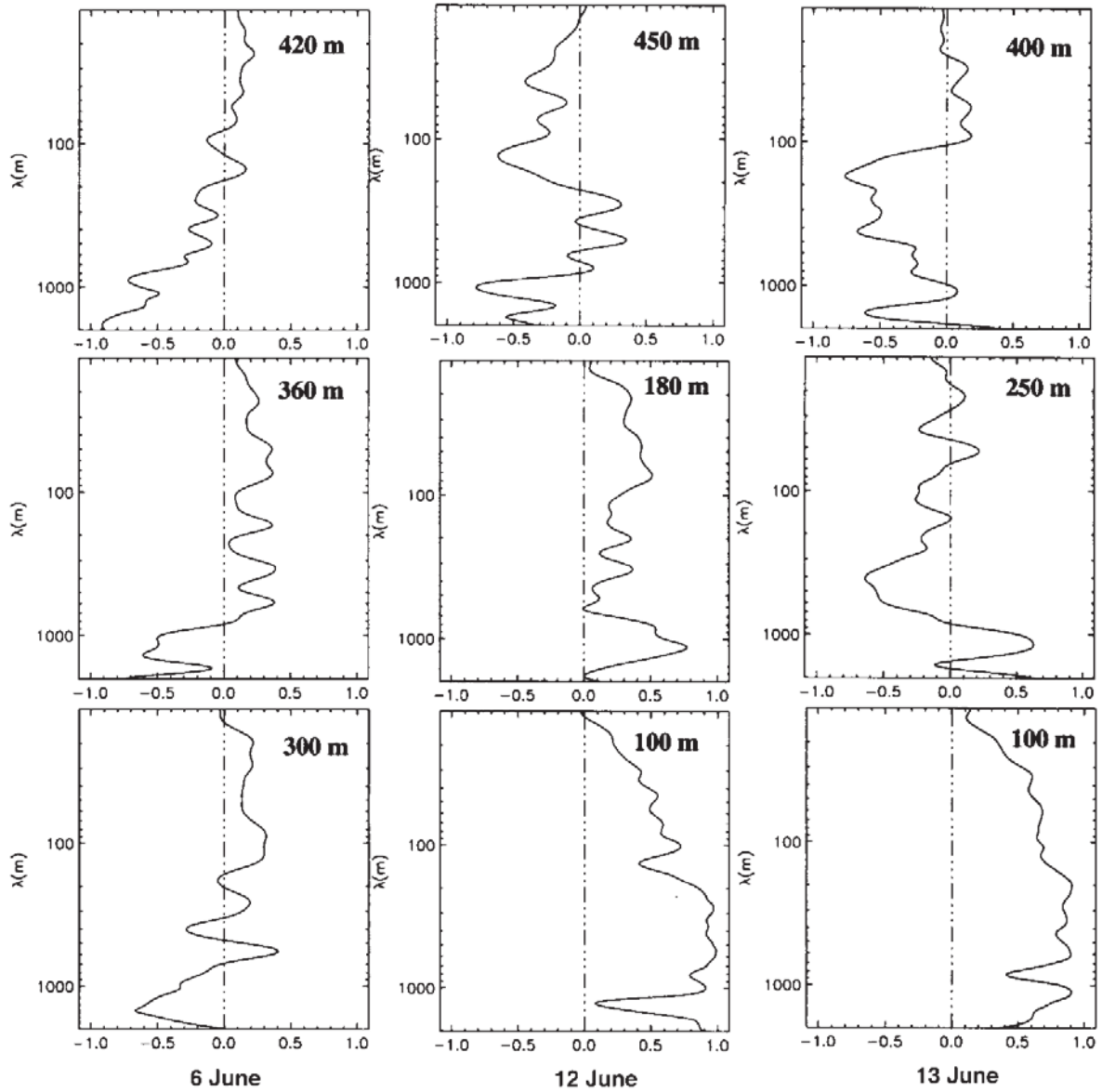


Figure 14. Same as Figure 13 but for parallel flight legs.

have a larger contribution of upward flux, because the major part of the leg is performed within a thicker boundary layer than for parallel legs. Figures 13 and 14 show the vertical evolution of this ratio for June 9, 12 and 13 for the normal and parallel runs, respectively. These figures clearly show a maximum positive ratio at the lowest level runs involving the largest scale range (levels 100 m a.s.l. and 150 m a.s.l.). This is typical for the surface layer. Concerning the upper levels, the ratio tends to decrease and reaches a negative value (which is clearly seen for the 600 m a.s.l. and 420 m a.s.l. on June 9, for the 450 m a.s.l. on June 12 and for the 600 m a.s.l. and 250 m a.s.l. on June 13). The level where the ratio is a minimum can be different in cross or parallel legs because of the topography, which reaches 180 m at the end of the cross leg. This negative ratio identifies the EZ showing the contribution of downward flux with respect to the total heat flux. Moreover, these diagrams show fairly well that the downward flux contributions lie in the large-scale range (typically about or greater than 1000 m). And, the scale range

TABLE I

Variance of the vertical velocity and kinematic sensible heat flux for the various flight legs perpendicular to the shore on June 9, 12 and 13, 1997.

Day	Time (UT)	Altitude (m a.s.l.)	$\overline{w'^2}$ ($\text{m}^2 \text{s}^{-2}$)	$\overline{w'\theta'}$ (K m s^{-1})
9th	1141	150	0.79	0.103
	1148	300	0.72	0.030
	1156	600	0.11	-0.010
12th	1307	150	0.51	0.037
	1313	300	0.37	0.017
	1325	450	0.33	-0.001
13th	1326	150	0.80	0.074
	1332	300	0.71	0.033
	1340	600	0.25	0.029

TABLE II

Same as Table I but for the flight legs parallel to the shore.

Day	Time (UT)	Altitude (m a.s.l.)	$\overline{w'^2}$ ($\text{m}^2 \text{s}^{-2}$)	$\overline{w'\theta'}$ (K m s^{-1})
9th	1213	300	0.50	0.002
	1221	360	0.48	0.001
	1230	420	0.40	-0.021
12th	1331	100	0.52	0.079
	1405	180	0.33	0.013
	1340	450	0.01	0.003
13th	1352	100	0.55	0.076
	1415	250	0.07	-0.005
	1401	400	0.02	-0.002

involved in the entrainment processes is smaller than that related to the surface but still covers a large-scale range (for example, from 3000 m to 200 m for June 9 at 420 m a.s.l.).

6. Conclusions

The goal of this paper was to demonstrate how the CWT can suggest new insights into the turbulence structure of the boundary layer. We used data collected with an instrumented aircraft during the BEMA97 campaign on the Spanish coast in June 1997. Three days, characterized by an established sea-breeze circulation, were studied. Vertically stacked flight legs were flown according to two tracks, perpendicular and parallel to the shoreline, respectively.

The wavelet transform is used for three different purposes: (1) When applied to a single time-series (for example, the turbulent vertical velocity), the wavelet energy scalogram diagnoses the location (in position and wavelength) of the main energetic turbulent structures; (2) when applied to coupled signals (vertical velocity and potential temperature, for instance), the wavelet cross-scalogram shows how the turbulent transfer varies in position and wavelength; and (3) when conditional sampling is combined with the wavelet cross-scalogram, it discriminates between upward and downward transfer.

The analysis of the normal flight legs showed that only the lowest legs (flown at about 100 m above the surface) follow the classical CBL scheme, with the most energetic wavelengths of the same order of magnitude as the local thickness of the boundary layer. On the same legs, the cross-scalogram of the heat flux clearly delineates the EZ on the various legs. Moreover, using the CWT, we presented a clear scheme that summarises the behaviour of downwards and upwards flux eddies within the bulk of the TIBL and the EZ. The legs parallel to the shore were performed somewhat later, which explains why the boundary layer has thickened with respect to the normal legs. As these samples are much more homogeneous than the previous ones, they do not exhibit horizontal variations in the wavelet energy spectra and cross-scalograms.

A parameter $\overline{r_k}$, which can be interpreted as a normalized cospectrum, was defined and calculated on the various time-series. It displays the degree of organization of the transfer, and the width of the wavelength range that contributes to the vertical flux. We showed that only the lowest flight legs (100 or 150 m a.s.l.) follow a classical turbulence scheme, with a wide range of scales involved in the cospectrum. In the EZ, the downward heat flux is transferred by a much narrower range of scales, reflecting coherent structures rather than developed turbulence. At the intermediate levels, both effects (surface upward sensible heat flux and upper-level downward heat flux) compete, and the result is a highly variable behaviour of $\overline{r_k}$.

The technique developed in this paper is useful in analysing the transfers in the boundary layer, mainly in inhomogeneous conditions. Although the work presented here focused on the sensible heat transfer, it could be performed on other quantities. An interesting application is the transport of pollutants in urban or industrial areas, mainly in regions where the boundary-layer structure is complicated

by surface variability (e.g., cities close to the sea; effects of terrain elevation; heat and moisture urban island).

Acknowledgements

The Biogenic Emission over the Mediterranean Area (BEMA) experiment was sponsored by the Commission of the European Union. The aircraft operation was coordinated by A. Lopez. We are grateful to Drs. Peter Bechtold, Yves Brunet, Alain Dabas, Stefano Galmarini and J.-F. Lamarque for their valuable comments during the preparation of this manuscript.

References

- Attié, J. L., Druilhet, A., Bénech, B., and Durand, P.: 1995, 'Analyse par ondelettes de signaux atmosphériques', in *Proceedings of the "Actes du Colloque de Mécanique des Fluides de Toulouse"*, Toulouse, 11–12 May, INP edn. Toulouse.
- Collineau, S. and Brunet, Y.: 1993, 'Detection of Turbulent Coherent Motions in a Forest Canopy. Part I: Wavelet Analysis', *Boundary-Layer Meteorol.* **65**, 357–379.
- Deardorff, J. W.: 1974, 'Three-Dimensional Numerical Study of Turbulence in an Entraining Mixed Layer', *Boundary-Layer Meteorol.* **7**, 199–226.
- Druilhet, A. and Durand, P.: 1997, 'Experimental Investigation of Atmospheric Boundary Layer Turbulence', *Atmos. Res.* **43**, 345–388.
- Druilhet, A., Attié, J.-L., De Abreau Sá, L., Durand, P., and Bénech, B.: 1994, 'Experimental Study of Inhomogeneous Turbulence in the Lower Troposphere by Wavelet Analysis', in Charles K. Chui, Laura Montefusco, and Luigia Puccio (eds.), *Wavelet: Theory, Algorithms, and Applications*, Vol. 5, Academic Press Inc., ISBN 0-12-174575-9.
- Durand, P., Frangi, J.P., and Druilhet, A.: 1988, 'Energy Budget for the Sahel Surface Layer during the ECLATS Experiment', *Boundary-Layer Meteorol.* **42**, 27–42.
- Farge, M.: 1992, 'Wavelet Transforms and their Applications to Turbulence', *Annu. Rev. Fluid. Mech.* **24**, 395–457.
- Galmarini, S. and Attié, J.-L.: 2000, 'Turbulent Transport at the Thermal Internal Boundary Layer Top: Wavelet Analysis of Aircraft Measurements', *Boundary-Layer Meteorol.* **94**, 175–196.
- Grossman, A. and Morlet, J.: 1984, 'Decomposition of Hardy Functions into Square Integrable Wavelets of Constant Shape', *SIAM J. Math. Anal.* **15**, 723–736.
- Hudgins, L. H., Friehe, C. A., and Mayer, M. E.: 1993, 'Wavelet Transform and Atmospheric Turbulence', *Phys. Rev. Lett.* **71**, 3279–3282.
- Kaimal, J. C. and Finnigan, J. J.: 1994, *Atmospheric Boundary Layer Flows: Their Structure and Measurement*, Oxford University Press, New York, NY, 289 pp.
- Lambert, D. and Durand, P.: 1999, 'The Marine Atmospheric Boundary Layer during SEMAPHORE. Part 1: Mean Vertical Structure and Non-Axisymmetry of Turbulence', *Quart. J. Roy. Meteorol. Soc.* **125**, 495–512.
- Mahrt, L.: 1991, 'Eddy Asymmetry in the Sheared Heated Boundary Layer', *J. Atmos. Sci.* **48**, 472–492.
- Seufert, G. (ed.): 1997, 'Bema, a European Commission Project on Biogenic Emission in the Mediterranean Area', *Atmos. Environ.* **31**(S1), 1–256.
- Torrence, C. and Compo, G. P.: 1998, 'A Practical Guide to Wavelet Analysis', *Bull. Amer. Meteorol. Soc.* **79**, 61–78.